FACTA UNIVERSITATIS
Series: **Mechanical Engineering**
https://doi.org/10.22190/FUME231003012F

Original scientific paper

NUMERICAL STUDY AND DESIGN OPTIMIZATION ON ENERGY ABSORPTION OF THIN-WALLED TUBE WITH A YOSHIMURA PATTERN

Yudong Fang[1,2], Weijian Han[2,3], Zhenfei Zhan[4], Li Huang[2,3]

[1]College of Mechanical and Vehicle Engineering, Chongqing University,
Chongqing, China
[2]College of Materials Science and Engineering, Nanjing Tech University, Nanjing, China
[3]Yangtze Delta Region Institute of Advanced Materials, Suzhou, China
[4]School of Mechatronics and Vehicle Engineering, Chongqing Jiaotong University,
Chongqing, China

Abstract. *This paper presents a numerical investigation and design optimization of the energy absorption of an origami tube. The arrangement of the tube's surface is inspired by a Yoshimura pattern. A numerical simulation model is developed in ABAQUS/Explicit to simulate the axial crushing of the origami tube. The simulation model is validated by comparing its deformation with the deformation observed in physical tests. Considering the limitations of existing single parametric analysis in the study of the origami tube with a Yoshimura pattern, the paper emphasizes a comprehensive parametric study, which includes a full factor analysis that considers the structural topological parameters, as well as a global sensitivity analysis that considers all the structural parameters. Furthermore, there has been limited reporting on structural optimization for thin-walled tubes with Yoshimura pattern. The paper also highlights multi-objective optimization for origami tubes with a Yoshimura pattern. The optimization aims to enhance energy absorption efficiency and minimize the peak crushing force. To address the computational demands, a surrogate model-based optimization approach is employed for the optimization problem. The optimization process results in a set of Pareto front solutions, offering a range of peak crushing force values from 151.5 to 288.69 kN and specific energy absorption values from 16.06 to 19.52 kJ/kg.*

Key words: *Origami tube, Parametric study, Design optimization, Surrogate model*

Received: October 03, 2023 / Accepted March 07, 2024

Corresponding author: Zhenfei Zhan
School of Mechatronics and Vehicle Engineering, Chongqing Jiaotong University, Chongqing 400044, China
E-mail: zhenfeizhan@cqjtu.edu.cn

1. INTRODUCTION

Thin-walled tubes have a wide range of applications in the automotive and aerospace industries as energy absorption devices [1]. In particular, in the design of passive vehicle safety systems, crash boxes are commonly employed as typical thin-walled structural components to ensure the crashworthiness of vehicle bodies. The crash box is designed to minimize damage to other key components, such as the front rail of the vehicle, in low-speed crashes, thereby improving maintenance costs and providing occupant safety in high-speed crashes. Consequently, when designing a thin-walled tube as the crash box, it needs to absorb more energy and exert a smaller crushing force on the front rail during dynamic impacts. Research indicates that the energy absorption characteristics of a thin-walled structure are closely related to the mode of crush deformation. Among various deformation modes, such as radial bending and tangential torsion, the desired mode in a crash scenario is axial progressive folding deformation, as it corresponds to the optimal energy absorption characteristics of a thin-walled tube [2].

Adding inducing grooves or inducing holes is an effective approach to achieve the desired deformation mode and decrease the crushing force [3-5]. In vehicle passive safety design, inducing grooves and holes are commonly arranged on the crash box, which is made of steel, while crash boxes made of aluminum alloy typically use inducing holes. Conical tubes are another typical type of tube that has been numerically and experimentally proven to perform well under axial and oblique impacts [6]. Novel designs based on conical tubes have been developed by combining design elements such as taper, variable thickness, and foam filler [7-9]. According to the research work of Najibi et al. [10], thin-wall tubes filled with lightweight foam take high specific energy absorption when the foam material is well chosen. Multi-cell thin-walled tubes have also attracted significant attention in the development of energy absorption devices. These tubes are formed by specific structures, such as holes or cross-shaped structures arranged in the cavity of the tube, extending from the top surface along the tube axis to the bottom surface. For example, a typical multi-cell tube is a quad tube with a centered cross connecting the four center points of the tube edges. Chen et al. [11] and Kim et al. [12] found that multi-cell tubes exhibit more stable deformation and higher specific energy absorption compared to traditional single-cell thin-walled tubes. Combining the characteristics of multi-cell thin-walled tubes and conical tubes, the multi-cell tapered thin-walled tube was developed. Googarchin et al. [13] studied the crashworthiness of multi-cell square tubes and multi-cell tapered tubes through theoretical derivation and numerical simulation, revealing that the tapered multi-cell tube exhibited better crashworthiness than the square tube under the same conditions.

Origami tube is considered a promising choice for designing energy absorption devices. Similar to origami, where the folding process of plastic hinges formed by two folding faces can be observed, the axial collapse deformation of a thin-walled tube can be approximated to an origami process. Numerical and experimental studies indicate that thin-walled tubes with origami patterns exhibit outstanding energy absorption, stable axial collapse modes, more uniform crushing load distribution, and low initial buckling force during the crushing process [14-16]. Aghamirzaie et al. [17] proposed a novel multi-layered origami thin-wall tube. Compared with the conventional octagonal tube, the proposed origami tube could achieve a 55% decrease in the initial peak force while maintaining the specific energy absorption. Zhai et al. [18] developed an origami honeycomb, which, when compared to traditional honeycomb structures, exhibits a more stable folding process during out-of-plane crushing.

Gaining insightful understanding of the effects of structural parameters on the performance of an origami tube is helpful in designing desired origami tubes with suitable layouts of origami patterns and appropriate parameters. Based on numerical simulation and physical test, Wickeler et al. [19] carried out a two-level and three-factor full factorial design of experiment to investigate the shape deformation mechanism of thin-walled tube with Miura-ori pattern. Zhou et al. [20] conducted a parametric study based on single-factor analysis to investigate the effects of geometric parameters on the energy absorption of an origami tube with diamond patterns. The parameters studied included the length and width of the tube, tube thickness, length of the unfolded origami pattern unit, and width of the folded lobe of the origami pattern unit. Yang et al. [21] examined the effects of thickness on the energy absorption of circular tubes, origami tubes with diamond patterns, and origami tubes with Yoshimura pattern. The specific energy absorption increases with increasing tube thickness. When the tubes have the same thickness, the origami tube with Yoshimura pattern exhibits the highest specific energy absorption among the three. Ye et al. [22] conducted a parameter analysis to investigate the effects of tube geometries and ply stacking sequence on the energy absorption behavior of an origami tube made of carbon-reinforced plastics. The existing parametric study on origami tubes mainly using single factor analysis, the coupling effects of parameters are still unknown. Furthermore, conducting a global analysis that covers a reasonable parameter range is necessary.

Structural optimization is a powerful approach to enhance the performance of designed tubes [23,24]. Baykasoğlu et al. [25] optimized a hybrid structure consisting of an aluminum square tube filled with a functionally graded lattice structure to improve the crashworthiness of the hybrid structure under multiple impact loading conditions. Surrogate models based on least square regression were used to reduce computational burden in the optimization process. Based on Polynomial Neural Networks and Evolutionary Algorithms, Najibi et al. [26] performed a multi-objective optimization to efficiently synthesize a thin-walled structure with a combination of circular and square sections. A set of Pareto solutions was yielded by minimizing peak crushing force and maximizing specific energy absorption.

Yang et al. [27] performed multiple-objective optimization for a multi-cell origami tube by reducing the initial peak force and the fluctuation of the loading-displacement curve under dynamic impact. Quadratic response surfaces were trained as surrogates of numerical simulations to reduce computational burden. Fiumarella et al. [28] presented a multiple-objective study on an origami tube with diamond patterns formed by carbon fiber/epoxy prepreg woven. The initial peak force and total energy absorption were optimized using a genetic algorithm. Surrogate models were employed in the optimization process to avoid extensive time-consuming simulations. More research on the optimization of energy absorption characteristics of origami tubes can be found in references [29-32].

As an extension of previous research work [21], this paper presents a numerical study and design optimization for the energy absorption of an origami tube with Yoshimura pattern. Different from the previous research work, which involved a simple single-factor analysis to investigate the effects of thickness, the current study involves a comprehensive parametric study. The parametric study includes a full factor analysis that considers the structural topological parameters, as well as a global sensitivity analysis that considers all the structural parameters. As there is a lack of reported research on structural optimization for thin-walled tubes with the Yoshimura pattern, a multi-objective optimization is then performed to maximize the specific energy absorption of the tube and minimize the peak crushing force. Surrogate models are employed to ensure optimization efficiency.

The remainder of this paper is organized as follows: Section 2 presents an origami tube with Yoshimura pattern. Section 3 describes the construction of a finite element analysis (FEA) model used to simulate the structural performance of the tube under quasi-static crushing. Section 4 presents a parametric study to investigate the effects of structural parameters on the performance of the origami tube. Section 5 describes a multiple-objective optimization based on surrogate models and a genetic algorithm to optimize the origami tube. The conclusions are provided in the last section.

2. ORIGAMI TUBE

The specific origami pattern examined in this study is the full-diamond pattern, also known as the Yoshimura pattern. As depicted in Fig. 1, the origami tube consists of isosceles triangular facets. The length of the tube is denoted as L. and it can be uniformly divided into multiple cells along the axial direction. The number of cells is represented as n_c. The cross-sectional shape of the tube, when viewed from the top, forms a regular polygon. The diameter of the origami tube, denoted as D, is defined as the diameter of the circumscribed circle of the regular polygon. The number of the edges of the regular polygon is denoted as n_e. The structural topology primarily depends on the design parameters n_c and n_e. In the case shown, n_c and n_e are equal to 4 and 6, respectively. A view of the intersection angle of two neighbored isosceles triangular facets along the axial direction, θ, and the base angle of the isosceles triangular facet, α is shown in Fig. 1(d). With the given L, D, n_e and n_c, intersection angle of two neighbored isosceles triangular facets along the axial direction, θ and the base angle of the isosceles triangular facet, α could be derived by Eqs. (1) and (2), respectively. The prefolding angle of the origami tube is the supplementary angle of θ.

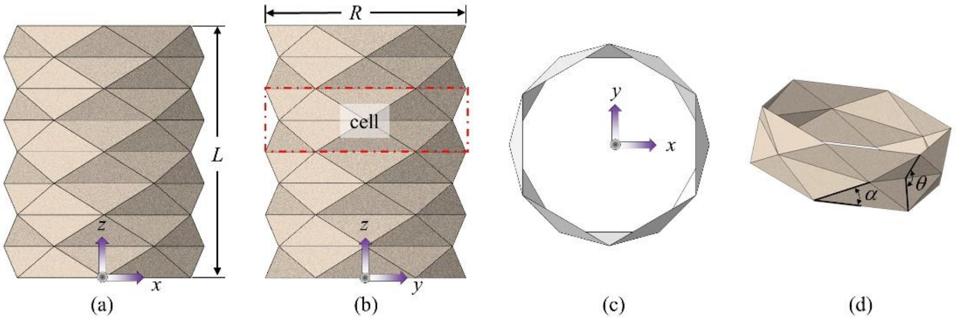

Fig. 1 Thin-walled tube with a Yoshimura pattern: (a) front view; (b) left view; (c) top view; (d) a view of intersection angle of two neighboured isosceles triangular facets along the axial direction, θ, and the base angle of the isosceles triangular facet, α

$$\theta = 2\arctan\frac{L}{Dn_c[1-\cos(\frac{\pi}{n_e})]} \tag{1}$$

$$\alpha = \arctan\frac{L}{Dn_c\sin(\frac{\theta}{2})\sin(\frac{\pi}{n_e})} \tag{2}$$

The generation of the origami tube could be summarized as:

1) Along the axis direction, $2n_c+1$ regular polygons with n_e edges are distributed as shown in Fig. 2(a). All regular polygons have the same circumscribed circle. The distance between two neighbored regular polygon in the axis direction is $L/(2n_e)$. The projections of two neighbored regular polygons in the x-y plane are shown in Fig. 2(b). If rotating one projection with an angle of φ, where $\varphi = \pi/n_e$, the two projections will coincide.

2) With the given L, D, n_e and n_c, the coordinates of all the endpoints in Fig. 2(a) could be derived when the Coordinate origin is coinciding with the center of the bottom edges of the origami tube.

3) Creating isosceles triangular facets with three endpoints, among whom two endpoints belongs to an edge of the i^{th} regular polygon, while the other one is the closest endpoints of the neighbored regular polygon. The creation of isosceles triangular facets is shown in Fig. 2(c).

In this paper, the base value of L, D, n_e and n_c are set to 100 mm, 90 mm, 6, and 4 respectively. The thickness of the tube, t, is set to 2 mm. The setting values of L and D are based on the geometry measurement of a vehicle crash box [33].

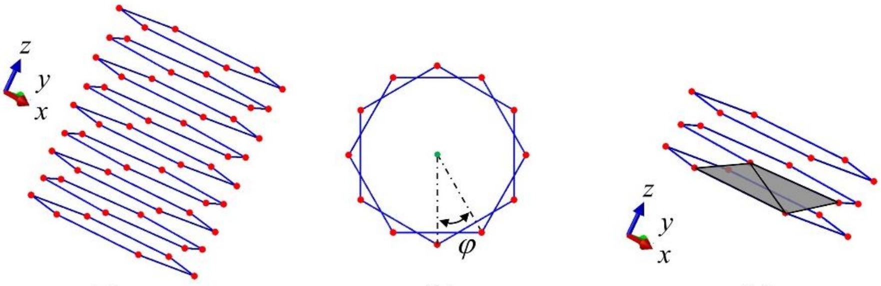

(a) (b) (c)

Fig. 2 A view of endpoint distribution and the creating of isosceles triangular facets: (a) a distribution of the endpoints of the origami tube; (b) projection of the endpoints on the x-y plane; (c) creation of two neighbored isosceles triangular facets

3. FINITE ELEMENT SIMULATION

Numerical simulation is an economical and reliable tool for studying the behavior of thin-walled structures [34,35]. In order to investigate the energy absorption and crushing force of the origami tube with Yoshimura pattern in an axial quasi-static crushing process, a FEA model is created using ABAQUS/Explicit. As depicted in Fig. 3(a), the bottom edges of the origami tube are fixed, while a constraint is applied to the top edges of the origami to ensure that the top edges of the origami tube undergo compression from top to bottom. Referencing to [21], the tube is compressed by a rigid body for a distance of 80 mm, with a speed of 8 m/s. To avoid initial penetration, the distance between the rigid body and the tube in the *z*-axis direction is set to 0.5 mm.

As shown in Figs. 3(b) and (c), the origami tube is discretized using doubly curved thin or thick shell elements with hourglass control, finite membrane strains, and reduced integration shell elements (S4R/S3R in Abaqus). The effects of mesh size on the energy absorption of the origami tube is analyzed as shown in Fig. 4(a). As the mesh size decreases, the energy absorption also decreases. When the mesh size is reduced from 2 mm to 1 mm, the energy absorption curves tend to overlap. The effects of mesh size on the displacement vs. force curve are analyzed, as shown in Fig. 4(b). It can also be observed that the two corresponding displacement vs. force curves have a high degree of overlap when the mesh sizes are set to 1.5 mm and 1 mm, respectively. Therefore, the mesh size is set to 1.5 mm. Self-contact is applied to the tube, while surface-to-surface contact is used to model the contact between the origami tube and the rigid plate. Referencing to [21], the friction coefficients for the contacts are set to 0.25. To avoid calculation error caused by the mesh size being smaller than the thickness of the surface, as recommended by ABAQUS User's guide, parameter 'scalethick=0.25' has been set on *SURFACE to allow a rescaling of the contact thickness where necessary for this surface.

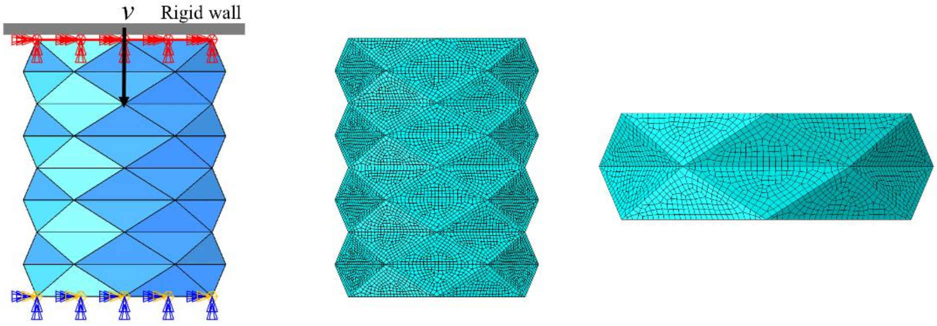

(a) (b) (c)

Fig. 3 Simulation model created in the Abaqus: (a) boundary condition and loading; (b) a view of the mesh; (c) an enlarged view of the meshing of a single cell

Since traditional manufacturing techniques are not applicable to the origami tube, additive manufacturing is a feasible option for fabricating it. In reference [21], raw brass was used to form the origami tube, and the material properties were determined through uniaxial tensile tests on samples fabricated by 3D printing [36]. The properties of the material applied to the simulation model are presented in Table 1.

Table 1 Material properties applied to simulation model [21]

Density	Poisson's ratio	Young's modulus	Yield strength	Ultimate tensile strength	Ultimate tensile strain
8494 kg/m3	0.35	110 GPa	165 MPa	385 MPa	0.2

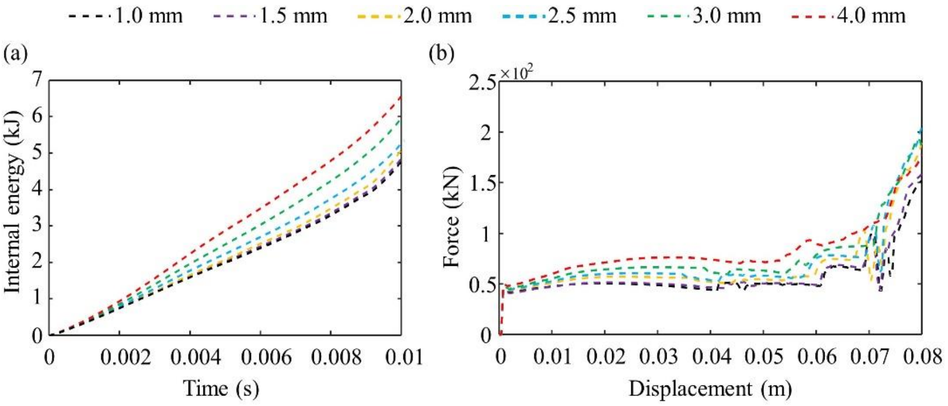

Fig. 4 Mesh size affects on the energy absorption and force-displacement curve of the origami tube: (a) internal energy-time curves; (b) force-displacement curves

The energy principle is always used to analyze the rationality of the model. The energy change along with the displacement of the rigid plate is presented in Fig. 5. As shown in the figure, the total energy introduced by the external work equals the sum of the internal energy and kinetic energy of the tube, which fits the principle of conservation of energy. The ratio of artificial strain energy (ALLAE), an indicator of hourglass occurrence in hexahedral and shell meshes in Abaqus, to internal strain energy is below 5%, indicating that the effects of hourglass are within an acceptable level.

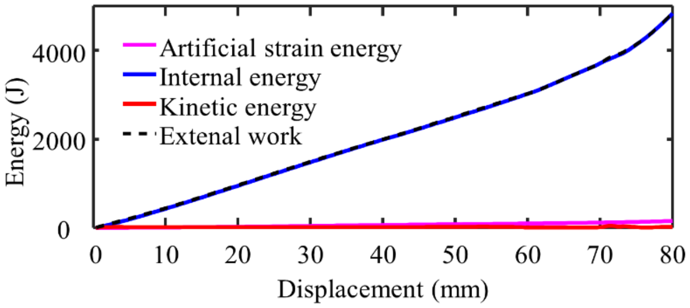

Fig. 5 Energy vs. the displacement of the rigid wall in the simulation

The crushing force and von Mises stress distribution versus displacement of the rigid plate are presented in Fig. 6. As shown in the figure, the initial peak force is introduced when the rigid plate starts contacting the origami tube. The stress is then transferred from the top edges of the tube to the bottom edges. The crushing force appears to be very stable as the displacement of the wall increases from 0 to 60 mm. However, when the tube is close to full deformation, the crushing force increases dramatically. The von Mises stress distribution is approximately symmetrical along the centerline of the origami tube. When the origami tube is fully deformed, there are 4 folding units, corresponding to 4 cells of the origami tube. The origami tube exhibits a very regular axial collapse in axial quasi-static crushing.

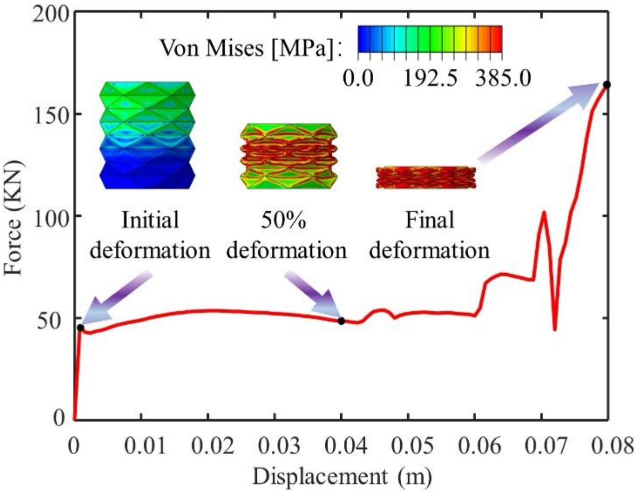

Fig. 6 Contour of the von Mises stress distribution and the crushing force vs. the displacement of the rigid wall

Yang et al. [21] performed a physical test to investigate the deformation behavior of the origami tube with a Yoshimura pattern. The simulation results could be compared to the physical test presented in Yang's work when the parameters *t*, *D*, n_e and n_c are set to 0.81 mm, 65.6 mm, 8, and 4, respectively. Fig. 7 displays the comparison of experimental and simulated deformation in the axial quasi-static crushing of an origami tube. Both the simulation and physical test indicate that buckling of the origami tube starts from the middle cell as shown in Fig. 7(a) and ends at the cell close to the rigid plate as shown in Fig. 7(c). The FE simulation and physical test exhibit consistency in terms of the deformation location and degree of deformation. Therefore, the FE model demonstrates good fidelity.

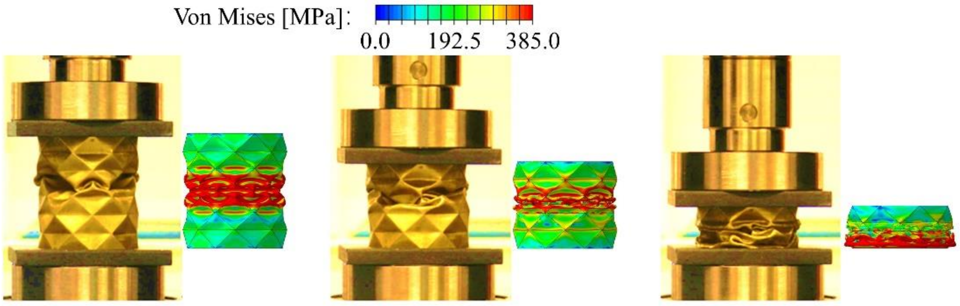

(a) Displacement of 24 mm (b) Displacement of 40 mm (c) Displacement of 72 mm

Fig 7 Simulation results vs. physical test corresponding to different displacement of the plate

4. PARAMETRIC STUDY

The parametric study is a process used to investigate the effects of a set of parameters on system responses or functions. It helps to gain insight into complex systems or processes and contributes to the development of new systems or designs [37,38]. In order to investigate the effects of design parameters on the energy absorption of the origami tube, a full factorial analysis considering n_e and n_c, as well as a global sensitivity analysis considering n_e, n_c, D, and t are conducted based on the data collected from FEA. The range of variables used in the study is listed in Table 2.

Table 2 Summary of the design parameters

Parameters	Lower bound	Upper bound	Type	Step
n_e	4	8	Discrete	1
n_c	3	7	Discrete	1
D	80 mm	90 mm	Continuous	-
t	1 mm	3 mm	Continuous	-

The specific energy absorption (*SEA*) and peak force (*PF*) are commonly used measurements to describe the energy absorption and crushing force of a thin-walled structure. The *SEA* is calculated using the following equation:

$$E = \int_0^s F(s)ds, \quad SEA = \frac{E}{M} \tag{3}$$

where s represents the displacement of the rigid plate in the z-axial direction. $F(s)$ is the crushing force of the origami tube on the rigid plate. E is total energy absorbed by the origami tube. M is the mass of the origami tube.

A full factor analysis is performed to investigate the effect of n_e and n_c on *SEA* and *PF*. Fig. 8 presents contour plots of *SEA* and *PF* as functions of n_e and n_c, considering different diameters and tube thicknesses of the origami tube. The gradient changes in color along the x-axis and y-axis reflect the effects of n_e and n_c on these measurements. Regardless of the combinations of D and t being considered, it is evident that for *SEA*, the color gradient along the x-axis is more pronounced, while the gradient along the y-axis is relatively subtle. This suggests that n_e has a greater influence on *SEA* compared to n_c. Increasing n_e leads to an increase in *SEA*, whereas increasing n_c slightly decreases *SEA*. This is because the larger value of n_e, the cross-section of the origami tube is more close to a circle. A circular cross-section, in geometric terms, achieves the maximum area with the minimum perimeter, making it perform better in terms of energy absorption capability.

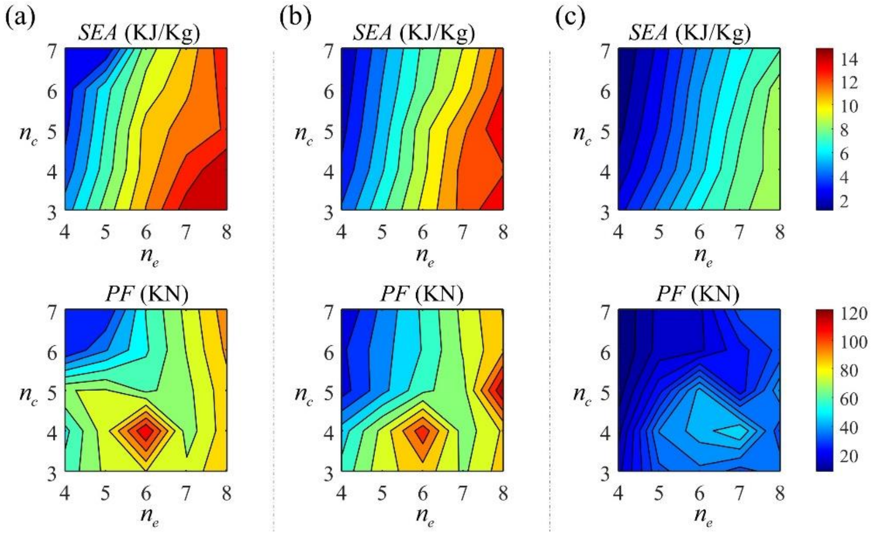

Fig. 8 Contour plots of the *SEA* and *PF* in different terms of n_e and n_c: (a) *D*=80 mm, *t*=2 mm; (b) *D*=90 mm, *t*=2 mm; (c) *D*=90 mm, *t*=1 mm

For *PF*, the color gradient changes are evident both along the *x*-axis and the *y*-axis, indicating that both n_e and n_c have noticeable effects on *PF*. The influence law is complex because of the interaction between n_e and n_c. This is because both n_e and n_c affects the prefolding angle of the origami tube, according to Eq. (1). The larger the value of n_c or the smaller the value of n_e, the larger the prefolding angle of the origami tube. The larger the prefolding angle, the easier of the origami tube to be crushed, resulting in a smaller peak crushing force. There is an interaction term of n_e and n_c in Eq. (1), indicating the effects of n_e and n_c could be complex. When n_c equals 6 or 7, the *PF* increases along with the increase of n_e. But when n_c is below 5, the *PF* fluctuates along with the change of $n_{e.}$

Furthermore, comparing Figs. 8(a) and (b), it can be concluded that the effects of *D* on *SEA* and *PF* are not significant. Although the value of *D* has been changed from 80 mm to 90 mm, the color distributions in the two figures are highly similar. In contrast, the color distributions in Figs. 8(b) and (c) differ significantly, indicating that the thickness of the tube, *t*, can have noticeable effects on both *SEA* and *PF*. The change of color distribution results from the thickness of the tube being changed from 2 mm to 1 mm. The thicker the origami tube, the earlier it will be fully compressed, resulting in a higher peak crushing force.

Sobol sensitivity analysis is a widely used global analysis method for investigating the effects of parameters on system responses. Herein, a global sensitivity analysis-based parametric study is conducted using the given parameter ranges listed in Table 2. Since Sobol sensitivity analysis requires a large number of samples, performing the analysis directly based on the FE simulations would result in a computationally expensive process. To overcome this challenge, surrogate models are recommended as an alternative approach to improve efficiency [39,40].

In this paper, instead of using the time-consuming FEA model, Kriging models with Gaussian correlation function and second-order polynomial function as global approximations are trained to predict *SEA* and *PF*. A total of 200 training samples are prepared by using optimal Latin hypercube sampling method and FE simulations. The accuracy of the surrogate models is evaluated using 10-fold cross-validation, with the R square metric providing an objective and intuitive evaluation of global accuracy. The R square values for the surrogate models built to predict *SEA* and *PF* are 0.986 and 0.943, respectively.

Fig. 9 presents the validation results of the surrogate models. As shown in Fig. 9, the red lines are perfect fitting lines. The scatters are predictions of the surrogate model vs. predictions of the FE model. The scatters located on the perfect fitting lines denote the surrogate model has the same prediction values as the FE model. The more scatters located on or near the perfect fitting line, the higher accuracy of the surrogate model. The R square value is closer to 1, the higher accuracy of the model. According to the distribution of scatters and R square values, all the surrogate models are acceptable to provide data support in a sensitivity analysis.

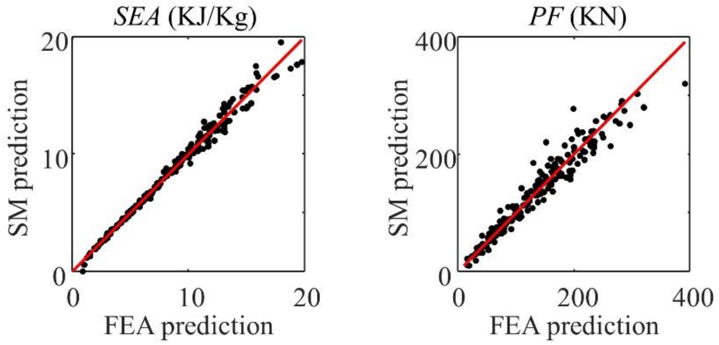

Fig. 9 Surrogate model (SM) predictions vs. FEA predictions

Referring to [41], Sobol sensitivity analysis under the support of surrogate models is performed. In this global sensitivity analysis, the total number of sample is set to 10^4. Fig. 10 shows the main effect of a single parameter (first-order indice) and the interaction effect of two parameters (second-order indice). The values on the main diagonal represent the main effects of the parameters, while the other values represent the interaction effects of two parameters. A threshold of 0.01 is set to judge the parameter is sensitive or not, while a threshold of 0.1 is set to judge a sensitive parameter is highly sensitive or not [42]. According to the sensitivity analysis results, *SEA*, is highly sensitive to n_e and *t*. In addition, *SEA* is sensitive to *D* and n_c. *PF* is only highly sensitive to *t*. n_e and n_c are sensitive parameters in determining *PF*. n_e and *t* have the most significant effects on *SEA* and *PF*, respectively. The *SEA* and *PF* are also sensitive to the interaction effect of n_e and *t*. In addition, *PF* is sensitive to the interaction effect of n_e and n_c. The ranking of the first four parameters that affect *SEA*, from small to large, is as follows: n_e, *t*, n_c and *D*, while the ranking of the first four parameters that affect *PF*, from small to large, is as follows: *t*, n_e, interaction between n_e and n_c, *and* n_c.

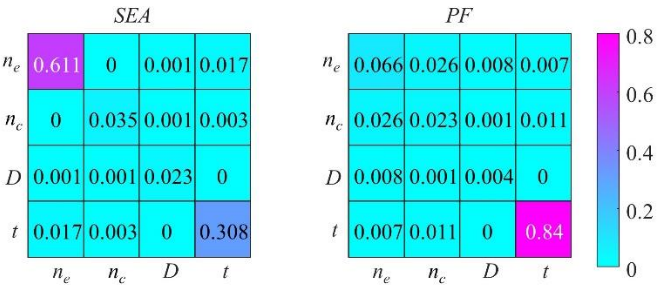

Fig. 10 First-order effects and interaction effects

5. OPTIMIZATION

In this section, multi-objective optimization is performed to determine the preferred n_e, n_c, D and t. The optimization objectives are to maximize *SEA* and minimize the *PF*, while satisfying the constraint on the energy absorption ($E \geqslant 9$ kJ). The optimization formulation is summarized as follows:

$$\begin{aligned}&\text{Find: } n_e, n_c, D, \text{ and } t,\\&\text{To minimize: } PF \text{ and } \frac{1}{SEA},\\&\text{Subject to: } E \geq 9\text{KJ}\end{aligned} \tag{4}$$

The range of the parameters that need to be optimized is provided in Table 2. The Nondominated Sorting Genetic Algorithm (NSGA-II) has been proven to be an effective method for solving multi-objective optimization problems in various domains, including engineering, finance, and data science [43]. In this paper, NSGA-II is employed to search for optimum designs that address the specific optimization problem in Eq. (4). The population size and the number of generation are set to 40 and 100, respectively. In the optimization process, instead of calling FE simulations, the surrogate models built in section 4 are used to improve optimization efficiency. To address the errors introduced by surrogate models, an adaptive optimization strategy is introduced as: Using FE simulation to validate the Pareto solutions obtained from the i^{th} round optimization. If the relative error of the responses of all Pareto solutions are below 0.01 and the solutions meet constraint conditions, the adaptive optimization is converged. Otherwise, the Pareto solutions will be added to the training sample set to update the surrogate models. The updated surrogate model will be used in the $i+1^{\text{th}}$ round of optimization. Totally 15 rounds of optimization have been performed to get the adaptive optimization converged and yield a set of Pareto front solutions as shown in Fig. 11. Due to the inclusion of discrete variables n_e and n_c in the optimization process, the Pareto front is not smooth. In Fig. 11, Three typical Pareto front solutions are marked as A, C, and B, corresponding to the solution with minimum peak force, the solution with the maximum specific energy absorption, and the compromised solution, respectively. The compromise solution is selected by adapting a Utopia point-based decision strategy from the Pareto solution set. The decision strategy based on the Utopian point can be referred to in [37,44].

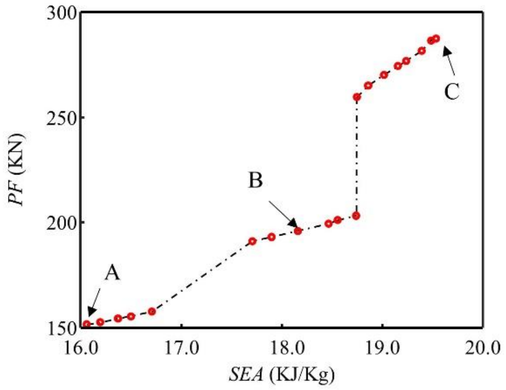

Fig. 11 Pareto front solutions and three typical Pareto front solutions marked marked as A, B, and C

Table 3 shows the summary of the three typical Pareto solutions and the corresponding responses obtained by FEA. All the Pareto solutions meet the constraint condition. The *PF* range of the Pareto solutions is from 151.5 kN to 288.69 kN, while the *SEA* range is from 16.06 kJ/kg to 19.52 kJ/kg. All three typical Pareto solutions prefer an origami tube with a high value of n_e , and a small value of n_c. In addition, all three typical Pareto solutions prefer to have a thick thickness and a small diameter for the designed origami tube.

Table 3 Summary of the Pareto front solutions

Parameters	Solution A	Solution B	Solution C
n_e	8	8	7
n_c	4	3	3
D (mm)	80	80	80
t (mm)	2.71	2.67	2.87
E (kJ)	9.33	10.24	11.89
PF (kN)	151.50	196.73	288.69
SEA (kJ/kg)	16.06	18.15	19.52

Fig. 12 displays the Von Mises stress distribution of the Pareto solutions vs. the deformation of the rigid plate. As all three origami tubes are symmetrical, the stress distribution is also symmetrical. The origami tube A starts its collapse from the bottom area of the tube, while the origami tubes B and C start their collapse from the top area and middle area of the tube, respectively. The final configurations of the three origami tubes are quite different. The obvious difference between origami tube A and origami tube B is the number of cell of the origami tube, n_c, indicating n_c could have effect on the sequence of deformation and the finial configuration of the origami tube. Observed from the final configuration, origami tube C has three fully folded units, which correspond to the three cells of the origami tube, indicating that this origami tube exhibits good axial progressive folding. However, we cannot find the same number of folded units as the number of cells in origami tubes A and B from their final configurations. From the view of deformation mode, the origami tube C could be the best solution among the three typical Pareto.

solutions.

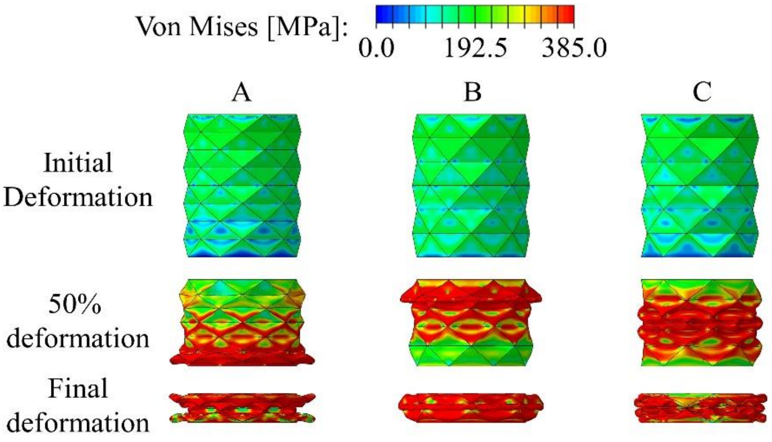

Fig. 12 Von Mises stress distribution of origami tubes corresponding to the three typical Pareto solutions vs. the deformation of the rigid plate

Fig. 13 displays the crushing force of the three typical origami tube vs. the displacement of the rigid plate. The three curves have similar trending when the displacement of the rigid plate is below 0.02 m. When the displacement of the rigid plate is close to 0.08 m, the crushing force of the tube C increase dramatically, while the crushing force of the origami tubes A and B on the rigid plate decrease and then slightly increase. This because the tube C is close to fully compressed as it has thicker thickness, while tubes A and B still have space to undertake the axial compression. When the origami tubes A and B trend to be fully compressed, their crushing forces start to increase slightly. From the view of crushing force control, the origami tubes A and B outperform origami tube C as the crushing force curves of the two origami tubes are more gentle.

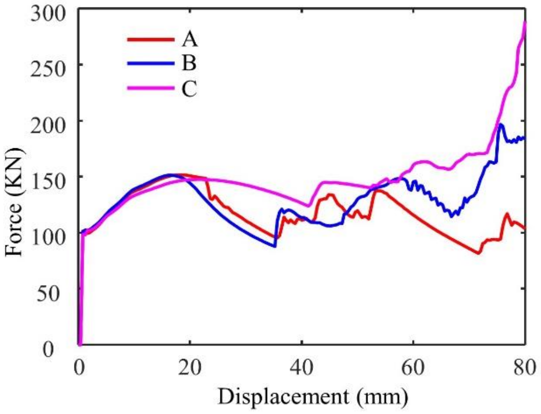

Fig. 13 The displacement of the plate vs. the crushing force corresponding to the three typical Pareto front solutions

6. CONCLUSION

This paper presents a numerical study and design optimization of an origami tube with Yoshimura pattern under axial compression. A FEA model was developed in Abaqus to simulate the axial quasi-static crushing process of the origami tube. The effects of structural parameters that govern the topological shape of the tube, such as the number of edges in the tube section and the number of cells in the axial direction, on energy absorption were investigated through a comprehensive factor analysis. Additionally, a global sensitivity analysis based on surrogate models was conducted to explore the impact of these parameters on energy absorption and peak crushing force from a global perspective. Finally, an adaptive multiple-objective optimization, employing surrogate models and a genetic algorithm, was applied to optimize the origami tube. The following findings were observed:

1. High-accuracy surrogate models could be built to describe the numerical relationship between the structural parameters of the origami tube and the peak force and energy absorption obtained from FE simulation.
2. The energy absorption of the origami tube is not sensitive to the diameter of the origami, but is sensitive to the thickness of the tube, the number of the edges of the tube section, and the number of the cells.
3. The peak crushing force of the origami tube is highly sensitive to the thickness of the origami tube. Structural topological parameters n_e and n_c are sensitive parameters of peak crushing force of the origami tube.
4. Multi-objective optimization based on the surrogate models and genetic algorithm could be performed to synthesize the origami tube efficiently.

Future work mainly focuses on physical experiments to validate the optimal origami tubes under axial compression.

Acknowledgement: *Y.F. was supported by the China Scholarship Council. The ABAQUS finite element analysis software is licensed from Dassault Systèmes SIMULIA, as part of a Strategic Academic Customer Program between UC Irvine and SIMULIA.*

REFERENCES

1. Loughlan, J., 2018, *Thin-walled structures: advances in research, design and manufacturing technology,* CRC Press.
2. Huang, F., Zhou, X., Zhou, D., Tao, Y., 2023, *Crashworthiness analysis of bio-inspired hierarchical circular tube under axial crushing,* Journal of Materials Science, 58(1), pp. 101-123.
3. Yang, Z., Yu, Y., Wei, Y., Huang, C., 2017, *Crushing behaviour of a thin-walled circular tube with internal gradient grooves fabricated by SLM 3D printing*, Thin-Walled Structures, 111, pp. 1-8.
4. Gupta, N.K., 1998, *Some aspects of axial collapse of cylindrical thin-walled tubes*, Thin-Walled Structures, 32(1-3), pp. 111-126.
5. Li, Z., Yang, H., Hu, X., Wei, J., Han, Z., 2018, *Experimental study on the crush behaviour and energy-absorption ability of circular magnesium thin-walled tubes and the comparison with aluminium tubes*, Engineering Structures, 164, pp. 1-13.
6. Mamalis, A.G., Johnson, W., 1983, *The quasi-static crumpling of thin-walled circular cylinders and frusta under axial compression*, International Journal of Mechanical Sciences, 25(9-10), pp. 713-732.
7. Zhang, X., Zhang, H., 2015, *Relative merits of conical tubes with graded thickness subjected to oblique impact loads*, International Journal of Mechanical Sciences, 98, pp. 111-125.
8. Zhang, H., Zhang, X., 2016, *Crashworthiness performance of conical tubes with nonlinear thickness distribution*, Thin-Walled Structures, 99, pp. 35-44.

9. Ahmad, Z., Thambiratnam, D.P., Tan, A.C.C., 2010, *Dynamic energy absorption characteristics of foam-filled conical tubes under oblique impact loading*, International Journal of Impact Engineering, 37(5), pp. 475-488.
10. Najibi, A., Ghazifard, P., Alizadeh, P., 2021, *Numerical crashworthiness analysis of a novel functionally graded foam-filled tube*, Journal of Sandwich Structures and Materials, 23(5), pp. 1635-1661.
11. Chen, W., Wierzbicki, T., 2001, *Relative merits of single-cell, multi-cell and foam-filled thin-walled structures in energy absorption*, Thin-Walled Structures, 39(4), pp. 287-306.
12. Kim, H.S., 2002, *New extruded multi-cell aluminium profile for maximum crash energy absorption and weight efficiency*, Thin-Walled Structures, 40(4), pp. 311-327.
13. Mahmoodi, A., Shojaeefard, M.H., Googarchin, H.S., 2016, *Theoretical development and numerical investigation on energy absorption behaviour of tapered multi-cell tubes*, Thin-Walled Structures, 102, pp. 98-110.
14. Ma, J., You, Z., 2014, *Energy absorption of thin-walled square tubes with a pre-folded origami pattern - part I: geometry and numerical simulation*, Journal of applied mechanics, 81(1), 011003.
15. Li, Y., You, Z., 2019, *Origami concave tubes for energy absorption*, International Journal of Solids and Structures, 169, pp. 21-40.
16. Song, J., Chen, Y., Lu, G., 2012, *Axial crushing of thin-walled structures with origami patterns*, Thin-Walled Structures, 54, pp. 65-71.
17. Aghamirzaie, M., Najibi, A., Ghasemi-Ghalebahman, A., 2023, *Energy absorption investigation of octagonal multi-layered origami thin-walled tubes under quasi-static axial loading*, International Journal of Crashworthiness, 28(4), pp. 511-522.
18. Zhai, J., Zhang, D., Li, M., Cui, C., Cai, J., 2022, *Out-of-plane energy absorption and crush behavior of origami honeycomb*, Thin-Walled Structures, 181, 109966.
19. Wickeler, A.L., sm Sajid, A., Naguib, H.E., 2022, *Triangular-based origami: Modelling and testing the parameterized design for geometrical and mechanical analysis*, Thin-Walled Structures, 173, 108993.
20. Zhou, C., Jiang, L., Tian, K., Bi, X., Wang, B., 2017, *Origami crash boxes subjected to dynamic oblique loading*, Journal of Applied Mechanics, 84(9), 091006.
21. Yang, K., Xu, S., Shen, J., Zhou, S., Xie, Y.M., 2016, *Energy absorption of thin-walled tubes with pre-folded origami patterns: Numerical simulation and experimental verification*, Thin-Walled Structures, 103, pp. 33-44.
22. Ye, H., Ma, J., Zhou, X., Wang, H., You, Z., 2019, *Energy absorption behaviours of pre-folded composite tubes with the full-diamond origami patterns*, Composite Structures, 221, 110904.
23. Najibi, A., Ghazifard, P., Torkian, J., 2022, *On the crashworthiness optimisation of a new multi-corner tube under axial loading*, Ships and Offshore Structures, pp. 1-14.
24. Baykasoğlu, A., Baykasoğlu, C., Cetin, E., 2020, *Multi-objective crashworthiness optimization of lattice structure filled thin-walled tubes*, Thin-Walled Structures, 149, 106630.
25. Baykasoğlu, C., Baykasoğlu, A., Cetin, E., 2023, *Multi-objective crashworthiness optimization of square aluminum tubes with functionally graded BCC lattice structure filler*, International Journal of Crashworthiness, 29(1), pp. 80-94.
26. Najibi, A., Shojaeefard, M.H., Yeganeh, M., 2016, *Developing and multi-objective optimization of a combined energy absorber structure using polynomial neural networks and evolutionary algorithms*, Latin American Journal of Solids and Structures, 13, pp. 2552-2572.
27. Yang, K., Xu, S., Zhou, S., Xie, Y.M., 2018, *Multi-objective optimization of multi-cell tubes with origami patterns for energy absorption*, Thin-Walled Structures, 123, pp. 100-113.
28. Ciampaglia, A., Fiumarella, D., Niutta, C.B., Ciardiello, R., Belingardi, G., 2021, *Impact response of an origami-shaped composite crash box: Experimental analysis and numerical optimization*, Composite Structures, 256, 113093.
29. Zhu, X., Chen, A., Huang, Z., Chen, Z., Lin, Y., Li, Y., 2023, *Quasi-static compression response of the origami thin-walled structure*, Thin-Walled Structures, 183, 110376.
30. Ciampaglia, A., Fiumarella, D., Niutta, C.B., Ciardiello, R., Belingardi, G., 2021, *Impact response of an origami-shaped composite crash box: Experimental analysis and numerical optimization*, Composite Structures, 256, 113093.
31. Yao, S., Zhu, H., Liu, M., Li, Z., Xu, P., 2020, *Energy absorption of origami tubes with polygonal cross-sections*, Thin-Walled Structures, 157, 107013.
32. Zhang, P., Sun, Z., Wang, H., Xiang, X., 2022, *Performance Study of Origami Crash Tubes Based on Energy Dissipation History*, Energies, 15(9), 3109.
33. Fang, Y., Chen, T., Zhan, Z., Liu, X., Yu, H., Zhao, H., 2018, *Automotive Crashworthiness Design Optimization Based on Efficient Global Optimization Method*, 2018 SAE World Congress, Detroit, USA.
34. Abdullah, N.A.Z., Sani, M.S.M., Salwani, M.S., Husain, N.A., 2020, *A review on crashworthiness studies of crash box structure*, Thin-Walled Structures, 153, 106795.
35. Onyibo, E.C., Safaei, B., 2022, *Application of finite element analysis to honeycomb sandwich structures: a review*, Reports in Mechanical Engineering, 3(1), pp. 192-209.

36. Ren, X., Shen, J., Ghaedizadeh, A., Tian, H., Xie, Y.M., 2015, *Experiments and parametric studies on 3D metallic auxetic metamaterials with tuneable mechanical properties*, Smart Materials and Structures, 24(9), 095016.
37. Fang, Y., Huang, L., Zhan, Z., Huang, S., Liu, X., Chen, Q., Zhao, H., Han, W., 2022, *A framework for calibration of self-piercing riveting process simulation model*, Journal of Manufacturing Processes, 76, pp. 223-235.
38. Zhao, Y., Wu, J., Wang, T., Cui, X., Fu, X., 2023, *Cable Replacement Scheme for Low Tower Cable-Stayed Bridges Based on Sensitivity Analysis*, Tehnicki vjesnik/Technical Gazette, 30(5), pp. 1603-1610.
39. Fang, Y., Zhan, Z., Yang, J., Liu, X., 2017, *A mixed-kernel-based support vector regression model for automotive body design optimization under uncertainty*, ASCE-ASME Journal of Risk and Uncertainty in Engineering Systems, Part B: Mechanical Engineering, 3(4), 041008.
40. Lu, J., Zhan, Z., Liu, X., Wang, P., 2018, *Numerical modelling and model updating for smart laminated structures with viscoelastic damping*, Smart Materials and Structures, 27, 075038.
41. Fang, Y., Huang, L., Zhan, Z., Huang, S., Han, W., 2020, *Effect analysis for the uncertain parameters on self-piercing riveting simulation model using Machine Learning model*, 2020 SAE World Congress, Detroit, USA.
42. Tang, Y., Reed, P., Van Werkhoven, K., Wagener, T., 2007, *Advancing the identification and evaluation of distributed rainfall‐ runoff models using global sensitivity analysis*, Water Resources Research, 43(6), pp. 1-14.
43. Ding, F., Liu, S., Li, X., 2022, *Pareto optimality of centralized procurement based on genetic algorithm*, Tehnicki vjesnik/Technical Gazette, 29(6), pp. 2058-2066.
44. Gunantara, N., 2018, *A review of multi-objective optimization: Methods and its applications*, Cogent Engineering, 5(1), 1502242.